Phase diagram of the three-dimensional axial next-nearest-neighbor Ising model

A. Gendiar[1,2] and T. Nishino[2]
[1]*Institute of Electrical Engineering, Slovak Academy of Sciences, Dúbravská cesta 9, SK-842 39 Bratislava, Slovakia*
[2]*Department of Physics, Faculty of Science, Kobe University, Kobe 657-8501, Japan*
(Received 27 September 2004; published 7 January 2005)

The three-dimensional axial next-nearest-neighbor Ising model is studied by a modified tensor product variational approach. A global phase diagram is constructed with numerous commensurate and incommensurate magnetic phases. The devil's stairs behavior for the model is confirmed. The wavelength of the spin modulated phases increases to infinity at the boundary with the ferromagnetic phase. Widths of the commensurate phases are considerably narrower than those calculated by mean-field approximations.

DOI: 10.1103/PhysRevB.71.024404 PACS number(s): 75.10.Hk, 02.70.−c, 64.60.Fr, 64.70.Rh

I. INTRODUCTION

Periodically modulated magnetic structures have attracted scientific interest for several decades both experimentally and theoretically. A nontrivial phase diagram obtained by experimental measurements in cerium antimonide (CeSb) shows a variety of different commensurately ordered magnetic structures with the underlying lattice.[1,2] The three-dimensional (3D) $S=\frac{5}{2}$ axial next-nearest-neighbor Ising (ANNNI) model has been considered as a theoretical candidate for CeSb since it exhibits a rich structure when it is treated by mean-field approximation.[3] The 3D $S=\frac{1}{2}$ ANNNI model is another example that shows a nontrivial spin modulated phase—the so-called devil's stairs. This model has been analyzed theoretically by various approaches, including high-temperature series expansions,[4,5] low-temperature series expansions,[6] mean-field approximations,[7] Monte-Carlo simulations,[8] an effective-field approximation,[9] free-fermion methods, a phenomenological renormalization, and other methods reviewed in Refs. 10 and 11. The Monte Carlo simulations have also been applied to the $S=\frac{1}{2}$ ANNNI model with a finite number of spin layers.[12] Recently, Henkel and Pleimling considered an anisotropic scaling at the Lifshitz point using the Wolff cluster algorithm and critical exponents have been calculated.[13]

The purpose of this paper is to clarify the phase structure of the 3D $S=\frac{1}{2}$ ANNNI model. Our interest is to study the spin modulated phases at intermediate temperatures, particularly, the stability of commensurate phases. For this purpose we apply a numerical variational method, the tensor product variational method (TPVA), to the model. In Sec. II we introduce the 3D ANNNI model and briefly discuss the variational background of the TPVA applied to the system. We present the numerical results in Sec. III, where we construct the global phase diagram of the model and analyze the spin modulated phases. We summarize the obtained results in Sec. IV. In the Appendix, a numerical self-consistent optimizing process is reviewed and efficiency of the modified TPVA is discussed.

II. MODEL AND NONUNIFORM PRODUCT VARIATIONAL STATE

We study the $S=\frac{1}{2}$ ANNNI model on a simple cubic lattice with the size $L\times\infty\times\infty$ along the x, y, and z directions, respectively. The model is described by the lattice Hamiltonian

$$\mathcal{H} = -J_1\sum_{i,j,k}\sigma_{i,j,k}(\sigma_{i+1,j,k}+\sigma_{i,j+1,k}+\sigma_{i,j,k+1}) + J_2\sum_{i,j,k}\sigma_{i,j,k}\sigma_{i+2,j,k}, \tag{1}$$

where the subscripts i, j, and k of the Ising spin $\sigma=\pm1$ refer to the x, y, and z coordinates, respectively. The ferromagnetic interaction $J_1>0$ acts between the nearest neighbors and $J_2>0$ is the competing antiferromagnetic interaction between the next-nearest-neighbors imposed only in the x direction.

Figure 1 shows the layer-to-layer transfer matrix $\mathcal{T}$ to the z direction which connects two adjacent spin layers $[\sigma]$ and $[\overline{\sigma}]$ (each of the size $L\times\infty$ in the x and y directions). The transfer matrix can be exactly expressed as the product of partially overlapped local Boltzmann weights (cf. Fig. 1)

$$\mathcal{T}[\sigma|\overline{\sigma}] = \prod_{i=1}^{L-2}\prod_{j=-\infty}^{+\infty} W^{\mathrm{B}}_{i,j}\{\sigma|\overline{\sigma}\}. \tag{2}$$

We simplify the notations using a group of six spins

$$\{\sigma\} \equiv (\sigma_{i,j}\sigma_{i',j}\sigma_{i'',j}\sigma_{i,j'}\sigma_{i',j'}\sigma_{i'',j'}), \tag{3}$$

with the index rule $i'=i+1$, $i''=i+2$, and $j'=j+1$. The local Boltzmann weight $W^{\mathrm{B}}_{i,j}$ of the Hamiltonian in Eq. (1) has the following form:

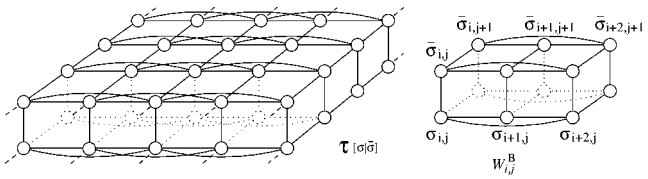

FIG. 1. The layer-to-layer transfer matrix $\mathcal{T}[\sigma|\overline{\sigma}]$ (left) illustrated in the case for $L=5$ and the local Boltzmann weight $W^{\mathrm{B}}_{i,j}\{\sigma|\overline{\sigma}\}$ (right).

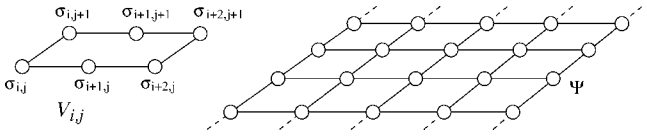

FIG. 2. Graphical representation of the local variational weight $V_{i,j}\{\sigma\}$ (left) used to construct the trial function Ψ (right) in the particular case for $L=5$.

$$W^{\mathrm{B}}_{i,j}\{\sigma|\overline{\sigma}\} = \exp\Bigg\{\frac{1}{k_{\mathrm{B}}T}\Bigg[\frac{J_1}{6}(\sigma_{i,j}\overline{\sigma}_{i,j} + \sigma_{i',j}\overline{\sigma}_{i',j} + \sigma_{i'',j}\overline{\sigma}_{i'',j} + \sigma_{i,j'}\overline{\sigma}_{i,j'} + \sigma_{i',j'}\overline{\sigma}_{i',j'} + \sigma_{i'',j'}\overline{\sigma}_{i'',j'} + \sigma_{i,j}\sigma_{i,j'} + \sigma_{i',j}\sigma_{i',j'} + \sigma_{i'',j}\sigma_{i'',j'} + \overline{\sigma}_{i,j}\overline{\sigma}_{i,j'} + \overline{\sigma}_{i',j}\overline{\sigma}_{i',j'} + \overline{\sigma}_{i'',j}\overline{\sigma}_{i'',j'}) + \frac{J_1}{8}(\sigma_{i,j}\sigma_{i',j} + \sigma_{i',j}\sigma_{i'',j} + \sigma_{i,j'}\sigma_{i',j'} + \sigma_{i',j'}\sigma_{i'',j'} + \overline{\sigma}_{i,j}\overline{\sigma}_{i',j} + \overline{\sigma}_{i',j}\overline{\sigma}_{i'',j} + \overline{\sigma}_{i,j'}\overline{\sigma}_{i',j'} + \overline{\sigma}_{i',j'}\overline{\sigma}_{i'',j'}) - \frac{J_2}{4}(\sigma_{i,j}\sigma_{i'',j} + \sigma_{i,j'}\sigma_{i'',j'} + \overline{\sigma}_{i,j}\overline{\sigma}_{i'',j} + \overline{\sigma}_{i,j'}\overline{\sigma}_{i'',j'})\Bigg]\Bigg\} \tag{4}$$

with k_{B} being the Boltzmann constant and the temperature T. For reasons of simplicity and brevity, we consider $J_1=1$ and $k_{\mathrm{B}}=1$ throughout all calculations.[14]

We consider a variational problem for the transfer matrix $\mathcal{T}[\sigma|\overline{\sigma}]$. For a given trial function $|\Psi\rangle$, the variational partition function per layer is given by

$$\lambda_{\mathrm{var}}(\Psi) = \frac{\langle\Psi|\mathcal{T}|\Psi\rangle}{\langle\Psi|\Psi\rangle} = \frac{\sum_{[\sigma],[\overline{\sigma}]}\Psi[\sigma]\mathcal{T}[\sigma|\overline{\sigma}]\Psi[\overline{\sigma}]}{\sum_{[\sigma]}(\Psi[\sigma])^2}. \tag{5}$$

The TPVA is a numerical variational method that assumes a trial function written by the product of local weights V. For the ANNNI model, Ψ is written in the product form of mutually overlapped local weights (cf. Fig. 2)

$$\Psi[\sigma] = \prod_{i=1}^{L-2}\prod_{j=-\infty}^{+\infty} V_{i,j}\{\sigma\}, \tag{6}$$

where we have used the simplified notation in Eq. (3).

In order to study nonuniform spin modulated phases, the local variational weights $V_{i,j}\{\sigma\}$ must be position dependent along the x direction. Each V thus contains $2^6=64$ adjustable parameters. Since we have written the trial function Ψ as well as the transfer matrix $\mathcal{T}$ in the product forms, both the numerator of Eq. (5),

$$\langle\Psi|\mathcal{T}|\Psi\rangle = \sum_{[\sigma],[\sigma']}\prod_{i=1}^{L-2}\prod_{j=-\infty}^{+\infty} V_{i,j}\{\sigma\}W^{\mathrm{B}}_{i,j}\{\sigma|\overline{\sigma}\}V_{i,j}\{\overline{\sigma}\}, \tag{7}$$

and its denominator,

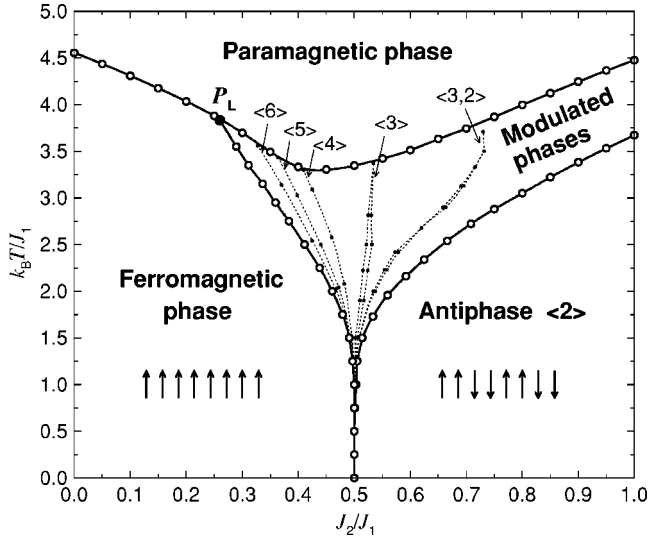

FIG. 3. The global phase diagram of the 3D ANNNI model obtained by the TPVA. The Lifshitz point P_{L} is denoted by the black circle. The dotted lines enclose extremely narrow commensurate phases.

$$\langle\Psi|\Psi\rangle = \sum_{[\sigma]}\prod_{i=1}^{L-2}\prod_{j=-\infty}^{+\infty}(V_{i,j}\{\sigma\})^2, \tag{8}$$

have also the product forms. Thus these quantities can be accurately calculated by means of renormalization techniques, particularly, we used the density matrix renormalization group (DMRG).[15,16]

III. RESULTS

Figure 3 shows the global phase diagram of the ANNNI model obtained by the TPVA. It consists of:

(i) a paramagnetic (disordered) phase;

(ii) a uniformly ordered ferromagnetic phase;

(iii) an antiphase with the periodic spin alignment $(\cdots\uparrow\uparrow\downarrow\downarrow\cdots)$ for which we use the notation $\langle 2\rangle$ in the following; and

(iv) a rich area of spin modulated phases.

The region of the spin modulated phases separates the antiphase from the paramagnetic phase. The paramagnetic, ferromagnetic, and the modulated phases meet at the Lifshitz point P_{L}. In our calculations, it is located at $J_2^{\mathrm{L}}/J_1=0.26$ and $k_{\mathrm{B}}T_{\mathrm{L}}/J_1=3.83$ and is in good agreement with the latest Monte Carlo calculations carried out by Pleimling and Henkel $J_2^{\mathrm{L}}/J_1=0.270(4)$ and $k_{\mathrm{B}}T_{\mathrm{L}}/J_1=3.7475(50)$ (from Ref. 13).

The resulting phase diagram does not contradict to previous knowledge of the model. The phase boundary lines separating the ferromagnetic phase, the paramagnetic phase, the antiphase, and the spin modulated phases are in good agreement with the phase boundaries obtained by the Monte Carlo calculations.[8] We found new features of the model in the region of the modulated phases, where the Monte Carlo simulations have not yielded a satisfactory answer. Our results are thought of as a supplement to the achievements

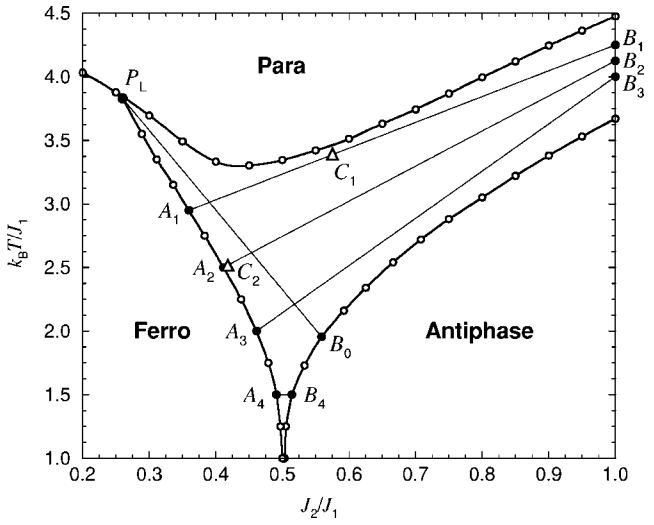

FIG. 4. The five selected lines A_1B_1, A_2B_2, A_3B_3, P_LB_0, and A_4B_4 in the region of modulated phases. The points C_1 and C_2 are marked by the white triangles

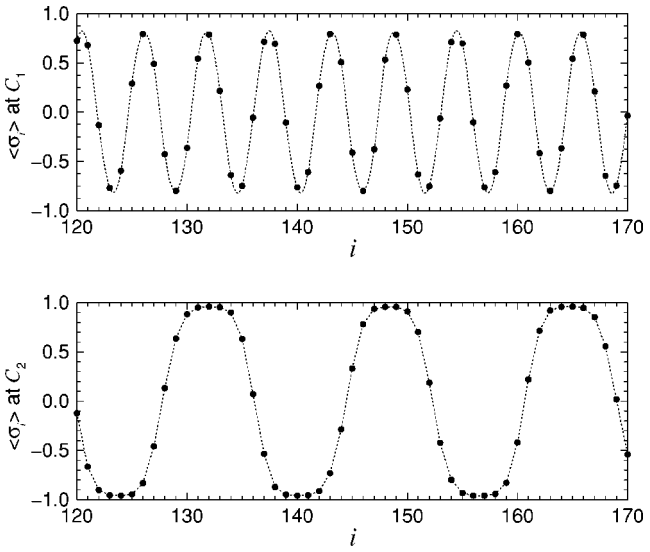

FIG. 5. The spontaneous magnetization $\langle\sigma_i\rangle$ vs the position i on the lattice in the x direction calculated at C_1 (the upper graph) and at C_2 (the lower one) with the lattice size $L=401$. In order to show the data in detail, we plot $i=120,\ldots,170$.

computed by the mean-field approximations[7,9] at higher temperatures and by the low-temperature series expansions valid at low temperatures $k_BT/J_1 \ll 4$.[6]

In the rest of this section, we focus on the region of the modulated phases that contains a multitude of various commensurate and incommensurate phases. For example, in Fig. 3 we plotted a few narrow areas of typical commensurate phases such as $\langle 3,2\rangle=(\cdots\uparrow\uparrow\uparrow\downarrow\downarrow\cdots)$, $\langle 3\rangle=(\cdots\uparrow\uparrow\uparrow\downarrow\downarrow\downarrow\cdots)$, $\langle 4\rangle=(\cdots\uparrow\uparrow\uparrow\uparrow\downarrow\downarrow\downarrow\downarrow\cdots)$, etc. all enclosed by the dotted lines. Note that the widths of these phases are substantially narrower compared to the mean-field approximation[7] and the effective-field approximation.[9]

A. Wavelength analysis

We first explain the relation between the conventional notation and the average modulation wavelength λ. The antiphase $\langle 2\rangle=\uparrow\uparrow\downarrow\downarrow\uparrow\uparrow\downarrow\downarrow$ has periodicity of four lattice sites, thus $\lambda=4$. Another example is the high-order commensurate phase $\langle 3,(3,2)^2\rangle$ which represents the periodic spin sequence $(\uparrow\uparrow\uparrow\downarrow\downarrow\downarrow\uparrow\uparrow\downarrow\downarrow\downarrow\uparrow\uparrow)$ and yields $\lambda=26/5$.

We calculate the spin modulations along five representative lines as depicted in Fig. 4 with their ending points listed in Table I. When we obtain the spontaneous magnetization (spin polarization) $\langle\sigma_i\rangle$, we compute the corresponding wavelengths by means of the Fourier transform.

TABLE I. The positions of the points depicted in Fig. 4.

Point	J_2/J_1	k_BT/J_1	Point	J_2/J_1	k_BT/J_1
P_L	0.2600	3.83	B_0	0.555	1.9812
A_1	0.3560	2.95	B_1	1.000	4.2500
A_2	0.4113	2.50	B_2	1.000	4.1250
A_3	0.4605	2.00	B_3	1.000	4.0000
A_4	0.4908	1.50	B_4	0.514	1.5000
C_1	0.5750	3.3921	C_2	0.418	2.5185

Figure 5 shows the spin polarizations $\langle\sigma_i\rangle$ at two parameter points: C_1 on the line A_1B_1 and C_2 on A_2B_2. These two points are chosen near the phase boundaries. The spin polarization at C_1 exhibits the commensurate phase $\langle 3^5,2\rangle \equiv(\cdots\downarrow\downarrow\downarrow\uparrow\uparrow\uparrow\downarrow\downarrow\downarrow\uparrow\uparrow\uparrow\downarrow\downarrow\downarrow\uparrow\uparrow\cdots)$ with the average modulation wavelength $\lambda=17/3$ (the upper graph). The lower graph shows the commensurate phase at C_2 with $\lambda\approx 16.7$ on the same region along the x direction.

Now, we give a brief discussion on the influence of boundary conditions imposed to the system on the resulting spin polarization. In Fig. 6 we plot $\langle\sigma_i\rangle$ for three different types of the boundary conditions. We consider a lattice with the size $401\times\infty\times\infty$ and analyze the data at C_2. On the upper graph, the spin polarization is calculated for the fixed boundaries on the left end (the spins are aligned to the "up" direction) and the free boundaries on the right end. The Fourier transform applied to the whole region $i=0,1,\ldots,400$ yields $\lambda=16.7\pm0.53$. On the intermediate graph, the parallel fixed boundary conditions on both sides are imposed (the spins are aligned "up" at the ends). It gives $\lambda=16.7\pm0.41$. Finally, the lower graph shows the antiparallel fixed boundaries ("up" on the left end and "down" on the right end) with $\lambda=16.7\pm0.41$. The choice of the boundary conditions does not affect the numerical results significantly. The larger the lattice size considered, the less influence of the boundaries is obtained, especially, off of the phase boundaries.

In Fig. 7 we plot the wavelength with respect to J_2/J_1 calculated on the three lines A_1B_1, A_2B_2, and A_3B_3. The dotted line is a guide for the eye to point out this structure. Near the boundary with the ferromagnetic phase, the wavelength rapidly increases. This is contradictory to the known results coming from the mean-field approximation. The mean-field approximation yields the first-order transitions between ferromagnetic phase and the individual commensurate phases on the boundary line (in detail, see Ref. 7).

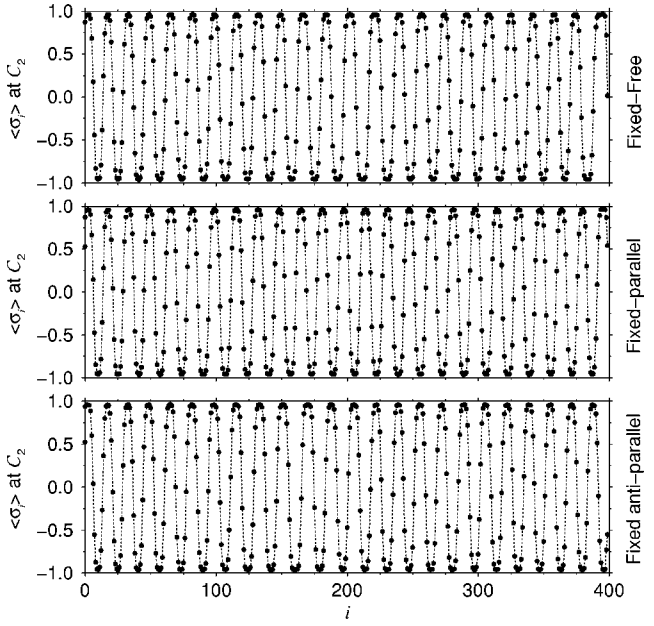

FIG. 6. The spontaneous magnetization obtained at C_2 for the lattice size $401\times\infty\times\infty$. The upper, middle, and lower graphs display $\langle\sigma_i\rangle$ for the three different boundary conditions.

In the inset of Fig. 7 we plot details of the wavelength λ in the vicinity of the commensurate phase ⟨3⟩. We observed that the commensurate phases ⟨3⟩, $\langle 3^2,2\rangle$, and ⟨3,2⟩ "lock-in" at small regions of J_2/J_1 (on the line A_3B_3) and the so-called "devil's stairs" behavior is observed.[10] On the contrary, the stairslike structure is not visible at higher temperatures, as seen on the line A_1B_1 near the paramagnetic boundary.

Figure 8 shows λ on the line from the point B_0 to the Lifshitz point P_L. The wavelength diverges toward the calculated Lifshitz point at $J_2/J_1=0.26$. The stairslike structure is revealed if we zoom in on the phase diagram. For this reason, we selected an area around the commensurate phases ⟨5⟩ and ⟨5,4⟩, where the wavelength locks-in as shown in the inset.

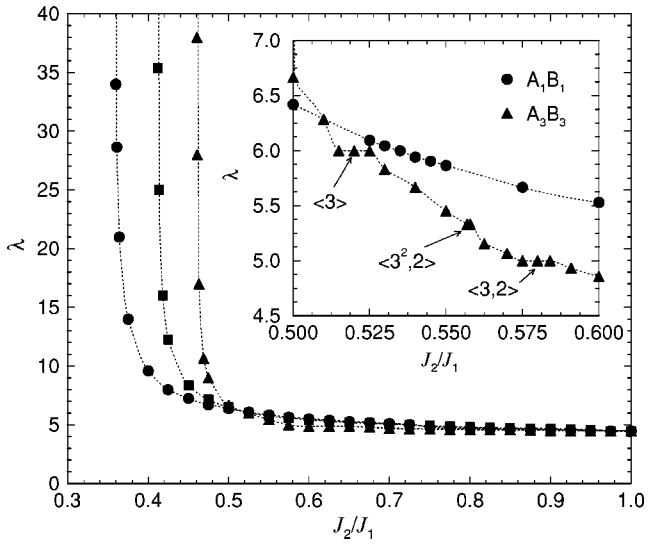

FIG. 7. The divergence of λ at the boundary with the ferromagnetic phase. The black circles, squares, and triangles, respectively, correspond to the selected points on the lines A_1B_1, A_2B_2, and A_3B_3. The inset shows behavior of λ around the commensurate phase ⟨3⟩.

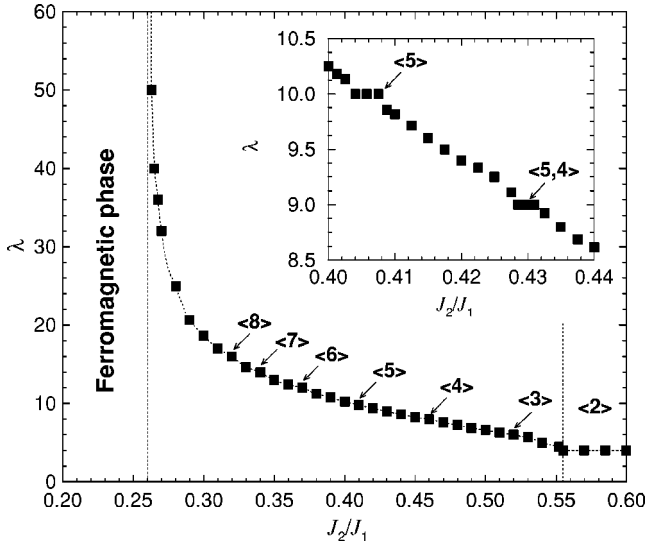

FIG. 8. The behavior of the wavelength λ on the line P_LB_0. Several commensurate phases with the integer value of λ are labeled. The inset shows the area around the commensurate phase ⟨5⟩.

B. Low temperature behavior

To compare our results with analytical predictions, particularly, with the low-temperature series expansions (LTSE),[6] we have selected the line A_4B_4 which corresponds to the temperature $k_BT/J_1=1.5$. The computed data are plotted in Fig. 9. The commensurate phase ⟨3⟩ (λ=6) locks-in and forms a well-visible plateau. Note that the mean-field

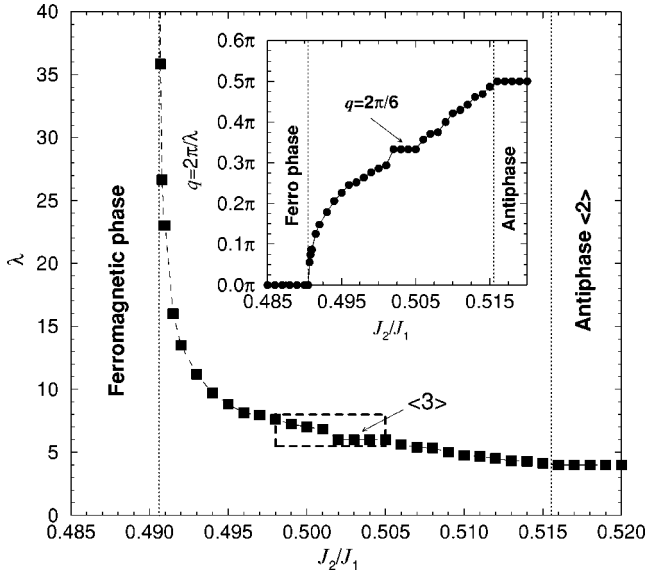

FIG. 9. The calculation of λ on the line A_4B_4 at the temperature $k_BT/J_1=1.5$. The dashed rectangle borders an area shown in Fig. 10. The inset illustrates the behavior of the corresponding wave vector q.

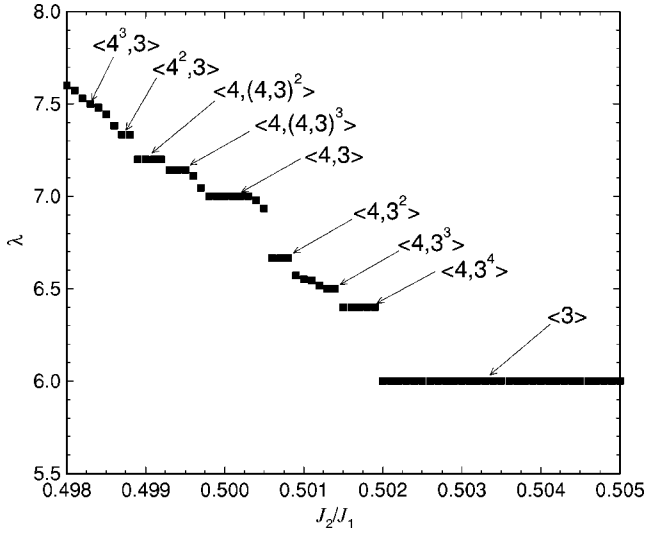

FIG. 10. The resulting devil's stairs with $\lambda \geqslant 6$ observed on the line A_4B_4.

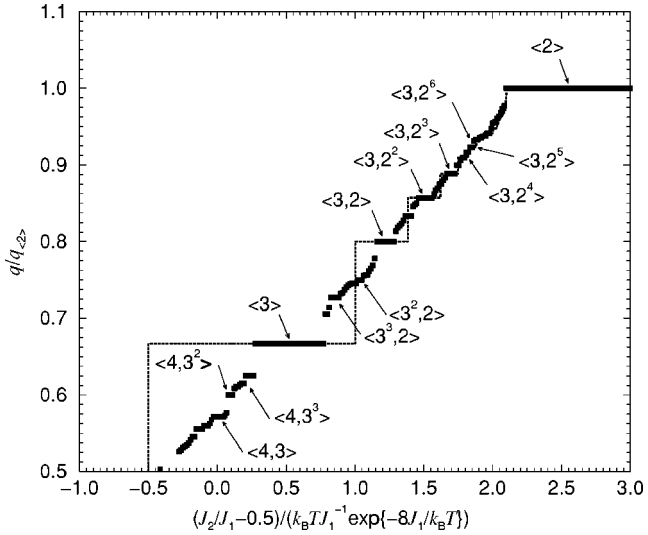

FIG. 11. Comparison of the numerical results at $k_BT/J_1=1.5$ (the black squares) with the low-temperature series expansions represented by the dashed stairslike curve (in Ref. 6).

calculations[7] do not exhibit any phases with $\lambda > 6$ at $k_BT/J_1 \lesssim 2$. It should be also noted that both the mean-field approximation (at higher temperatures) and the LTSE (at very low temperatures) do not result in the spring of phases with $\lambda > 6$ from the multiphase point $J_2/J_1=0.5$.

Figure 10 illustrates the stairslike structure of λ and corresponds to the magnified area shown by the dashed rectangle in Fig. 9. The commensurate phases lock-in at rational values of λ and are separated by high-order commensurate phases and (possibly) incommensurate ones. Several commensurate phases are denoted above the stairslike curve in Fig. 10.

The LTSE yields a spring of an infinity of the commensurate phases, such as $\langle 3 \rangle$ and $\langle 3,2^n \rangle$ for $n=1,2,3,\ldots$, which separate the ferromagnetic phase and the antiphase. The transition from the region of the spin modulated phases ($\lambda > 4$) to the antiphase ($\lambda = 4$) in our calculations does not contradict to the LTSE. The existence of additional intermediate phases, $\langle 3,2^n,3,2^{n+1} \rangle$ $n=1,2,3,\ldots$, at higher temperatures was later reported by the LTSE. Our results contain all these commensurate phases. Moreover, we found unpredicted phases. For example, the transition between the phases $\langle 3 \rangle$ and $\langle 3,2 \rangle$ is not of the first order as reported by the LTSE. We found that these two phases are separated by many commensurate phases, e.g., $\langle 3^n,2 \rangle$ and $\langle 3,(3,2)^{n+1} \rangle$ for $n=1,2,3,\ldots$ and the others of higher-orders as reported in Ref. 9. We obtained such rich spin modulated phases also for $\lambda > 6$, see Fig. 10.

In Fig. 11 we depict our numerical results calculated at $k_BT/J_1=1.5$ and compare them with the results obtained by the LTSE. The notation $q_{\langle 2 \rangle}$ corresponds to the antiphase wave vector $q=\pi/2$. Note that while the LTSE gives the first-order transition among individual commensurate phases, our calculations yield subsequent stairslike structures among them. Moreover, the LTSE calculations do not yield the commensurate phases with $\lambda > 6$.

We, therefore, conjecture that the "complete" devil's stairs structure exists at intermediate temperatures. The complete devil's stairs structure suggests there are no first-order transitions.[10]

Here, we summarize those commensurate phases which were obtained by the numerical analysis of this model. Between two main commensurate phases $\langle p \rangle$ and $\langle p+1 \rangle$, where $p=2,3,4,\ldots$, new high-order commensurate phases are present, such as $\langle p^{n-1},p+1 \rangle$, $\langle p,(p+1)^n \rangle$, $\langle p,(p,p+1)^{n-1} \rangle$, and $\langle (p,p+1)^n,p+1 \rangle$, with $n=2,3,4,\ldots$. Subsequently, the following higher-order commensurate phases were found $\langle (p^{n+1},p+1)^m,p^n,p+1 \rangle$ and $\langle [p,(p,p+1)^{n+1}]^m,p,(p,p+1)^n \rangle$, for $m=2,3,4,\ldots$, etc.

IV. SUMMARY

We applied the modified TPVA to the 3D ANNNI model and obtained the global phase diagram. The location of the Lifshitz point agrees with calculations performed by the high-temperature series expansions[4,5] and the recent Monte Carlo calculations.[13] The region of the modulated phases exhibits a very complex structure. We found that (1) the commensurate phases are substantially narrower than those reported so far, (2) the wavelength of the spin modulated (commensurate) phases diverges at the boundary with the ferromagnetic phase, (3) the commensurate phases merge at low temperatures tending toward the multiphase point $J_2/J_1=0.5$ and at low temperatures the wavelengths with $\lambda > 6$ are obtained, and (4) many (possibly infinity) phases have been found within the modulated phase, which have not yet been reported.

ACKNOWLEDGMENTS

A. G. thanks A. Šurda for an interesting discussion about the incommensurate phases in the ANNNI model. This work has been partially supported by the Grant-in-Aid for Scientific Research from Ministry of Education, Science, Sports and Culture (Grants No. 09640462 and No. 11640376) and by the Slovak Grant Agency, VEGA No. 2/7201/21 and

2/3118/23. A. G. is also supported by Japan Society for the Promotion of Science (P01192).

APPENDIX

1. Optimizing process for the local variational weights

We briefly describe the optimizing process of finding out the local variational weights in order to maximize Eq. (5). This optimization is based on a self-consistent equation in the TPVA to achieve the minimum of the free energy. Numerical details in the TPVA have been reported in Ref. 17.

In order to maximize the variational partition function in Eq. (5), by a proper tuning of the local variational weights V, we define two objects. One is the matrix object $\mathcal{B}$ that represents a punctured classical system[18] defined on the two-layer spin system which corresponds to the numerator $\langle\Psi|\mathcal{T}|\Psi\rangle$ of the variational partition function. It is defined as

$$\mathcal{B}_{i,0}\{\sigma|\overline{\sigma}\} = W^{\mathrm{B}}_{i,0}\{\sigma|\overline{\sigma}\} \sum_{[\tilde{\sigma}],[\tilde{\overline{\sigma}}]} \prod_{k\neq i} \prod_{\ell\neq 0} V_{k,\ell}\{\sigma\} \times W^{\mathrm{B}}_{k,\ell}\{\sigma|\overline{\sigma}\} V_{k,\ell}\{\overline{\sigma}\}. \tag{A1}$$

Analogously, the vector object $\mathcal{A}$ is the punctured system defined on the one-layer spin system,

$$\mathcal{A}_{i,0}\{\sigma\} = \sum_{[\tilde{\sigma}]} \prod_{k\neq i} \prod_{\ell\neq 0} V_{k,\ell}\{\sigma\} V_{k,\ell}\{\sigma\}. \tag{A2}$$

The configuration sums in Eqs. (A1) and (A2) are taken over all the spin variables σ except for the six at the center of the system. In particular, except for

$$\{\sigma\} = (\sigma_{i,0}\sigma_{i+1,0}\sigma_{i+2,0}\sigma_{i,1}\sigma_{i+1,1}\sigma_{i+2,1}) \tag{A3}$$

and analogously for $\{\overline{\sigma}\}$ in Eq. (A1). The notations $\Pi_{k\neq i}\Pi_{\ell\neq 0}$ exclude $V_{i,0}\{\sigma\}$ and $V_{i,0}\{\overline{\sigma}\}$ from the product. Having defined these two objects, the variational partition function can be transformed into the expression

$$\lambda_{\mathrm{var}} = \frac{\sum_{\{\sigma\},\{\overline{\sigma}\}} V_{i,0}\{\sigma\}\mathcal{B}_{i,0}\{\sigma|\overline{\sigma}\}V_{i,0}\{\overline{\sigma}\}}{\sum_{\{\sigma\}} V_{i,0}\{\sigma\}\mathcal{A}_{i,0}\{\sigma\}V_{i,0}\{\sigma\}}. \tag{A4}$$

Now, consider a variation of λ_{var} with respect to variations of the local variational weights

$$\frac{\delta\lambda_{\mathrm{var}}}{\delta\Psi} \equiv \sum_{i,j} \frac{\delta\lambda_{\mathrm{var}}}{\delta V_{i,j}}. \tag{A5}$$

Carrying out the extremal condition, $\delta\lambda/\delta V_{i,j}=0$, the self-consistent equation for the local variational weights $V_{i,j}$ is then obtained,

$$V^{\mathrm{new}}_{i,0}\{\sigma\} = \sum_{\{\overline{\sigma}\}} \frac{\mathcal{B}_{i,0}\{\sigma|\overline{\sigma}\}}{\mathcal{A}_{i,0}\{\sigma\}} V_{i,0}\{\overline{\sigma}\}. \tag{A6}$$

The improvement of V is performed as

$$V_{i,0}\{\sigma\} = V_{i,0}\{\sigma\} + \varepsilon V^{\mathrm{new}}_{i,0}\{\sigma\} \tag{A7}$$

through 64-parameter adjust. The self-consistent relation, Eq. (A6), is a nonlinear equation since $\mathcal{B}_{i,0}$ and $\mathcal{A}_{i,0}$ themselves depend on V. The convergence parameter ε controls the rate at which the improvement process of V is performed.

Consequently, we compute the free energy per strip

$$\mathcal{F}_{\mathrm{new}} = -k_{\mathrm{B}}T \ln \lambda_{\mathrm{var}} \tag{A8}$$

and compare it with the free energy $\mathcal{F}_{\mathrm{old}}$ calculated with the previous V.

TABLE II. The critical temperature T_{c} for the 3D Ising model ($J_2=0$). We calculate the relative errors ϵ with respect to T_{c} obtained by Monte Carlo simulations (Ref. 19).

Numerical method	T_{c}	ϵ/[%]
Mean-field approximation (Ref. 11)	6.000	33.0
Kramers-Wannier approximation (Ref. 20)	4.587	1.7
TPVA with 16 parameters (Ref. 17)	4.570	1.3
TPVA with 64 parameters	4.554	0.9
Monte Carlo simulations	4.512	

2. Efficiency of the algorithm

After the trial function $|\Psi\rangle$ is optimized, we calculate the spontaneous magnetization at a site

$$\langle\sigma_{i,j}\rangle = \frac{\langle\Psi|\sigma_{i,j}|\Psi\rangle}{\langle\Psi|\Psi\rangle}. \tag{A9}$$

Since the competing interactions exist only along the x direction, the system is translation invariant with respect to the y and z directions. Therefore the spontaneous magnetization $\langle\sigma_{i,j}\rangle$ is independent on j and we used $\langle\sigma_i\rangle$ instead.

In order to estimate the numerical accuracy of the improved TPVA, we compare the calculation of the critical

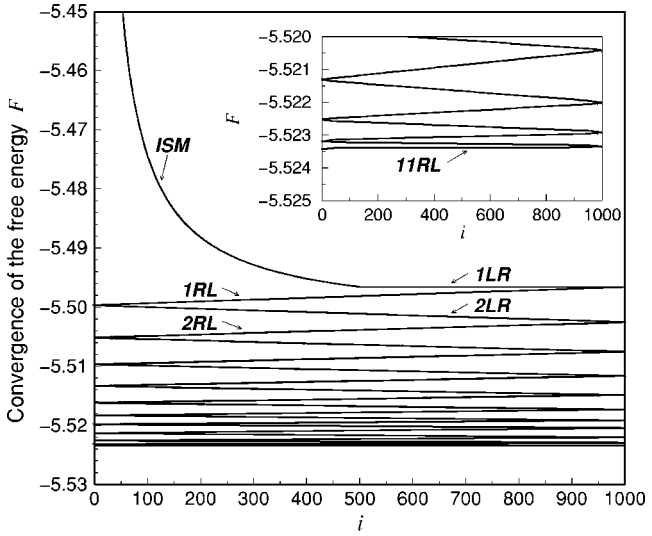

FIG. 12. Typical convergence process of the free energy $\mathcal{F}$ for the lattice size of $1001\times\infty\times\infty$. The inset shows a detailed view near the vicinity of the free energy minimum up to the eleventh sweep (11RL).

temperature T_c in the pure Ising model, i.e., when $J_2=0$, with other numerical methods. Table II summarizes the obtained T_c. It is obvious that the mean-field approximation overestimates T_c and does not give reliable results near the phase boundaries. The improved TPVA with the 64 variational parameters results in better T_c than the original TPVA with 16 parameters.[17,21]

We set up the convergence parameter $|\varepsilon|=10^{-2}$. Assuming any $|\varepsilon| \lesssim 10^{-2}$ is sufficient for the most cases.

In Fig. 12 we illustrate an example which demonstrates the systematic decay of the free energy during the DMRG sweeping process until it finally converges. After the DMRG infinite system method (ISM) is finished, the first left-right sweep (1LR) proceeds followed by the first right-left sweep (1RL) and so on. Each step of the finite system method decreases the free energy until its minimum is reached.

[1] P. Fisher, B. Lebech, G. Meier, B. D. Rainford, and O. Vogt, J. Phys. C **11**, 345 (1978).

[2] J. Rossat-Mignod, P. Burlet, J. Villain, H. Bartholin, Wang Tcheng-Si, D. Florence, and O. Vogt, Phys. Rev. B **16**, 440 (1977).

[3] J. von Boehm and P. Bak, Phys. Rev. Lett. **42**, 122 (1979).

[4] S. Redner and H. E. Stanley, J. Phys. C **10**, 4765 (1977); Phys. Rev. B **16**, 4901 (1977).

[5] J. Otmaa, J. Phys. A **18**, 365 (1985).

[6] M. E. Fisher and W. Selke, Phys. Rev. Lett. **44**, 1502 (1980); A. M. Szpilka and M. E. Fisher, *ibid.* **57**, 1044 (1986); M. E. Fisher and A. M. Szpilka, Phys. Rev. B **36**, 644 (1987); **36**, 5343 (1987).

[7] P. Bak and J. von Boehm, Phys. Rev. B **21**, 5297 (1980).

[8] W. Selke and M. E. Fisher, Phys. Rev. B **20**, 257 (1979); K. Kaski and W. Selke, *ibid.* **31**, 3128 (1985).

[9] A. Šurda, Phys. Rev. B **69**, 134116 (2004).

[10] P. Bak, Rep. Prog. Phys. **45**, 587 (1982).

[11] W. Selke, Phys. Rep. **170**, 213 (1988); W. Selke, in *Phase Transitions and Critical Phenomena*, edited by C. Domb and J. L. Lebowitz (Academic, New York, 1992), Vol. 15.

[12] W. Selke, M. Pleimling, and D. Catrein, Eur. Phys. J. B **27**, 321 (2002).

[13] M. Pleimling and M. Henkel, Phys. Rev. Lett. **87**, 125702 (2001); M. Henkel and M. Pleimling, Comput. Phys. Commun. **147**, 161 (2002).

[14] The numerical calculations were performed by the MIPSpro FORTRAN compiler on the RISC Unix cluster, the Intel FORTRAN Compiler on the Pentium4 Linux workstations, and the Compaq FORTRAN compiler on HPC-Alpha UP21264 Linux workstation.

[15] S. R. White, Phys. Rev. Lett. **69**, 2863 (1992); Phys. Rev. B **48**, 10 345 (1993).

[16] T. Nishino, J. Phys. Soc. Jpn. **64**, 3598 (1995).

[17] T. Nishino, K. Okunishi, Y. Hieida, N. Maeshima, and Y. Akutsu, Nucl. Phys. B **575**, 504 (2000); T. Nishino, K. Okunishi, Y. Hieida, N. Maeshima, Y. Akutsu, and A. Gendiar, Prog. Theor. Phys. **105**, 409 (2001); A. Gendiar and T. Nishino, Phys. Rev. E **65**, 046702 (2002); A. Gendiar, N. Maeshima, and T. Nishino, Prog. Theor. Phys. **110**, 691 (2003).

[18] M. A. Martín-Delgado, J. Rodriguez-Laguna, and G. Sierra, Nucl. Phys. B **601**, 569 (2001).

[19] W. Janke and R. Villanova, Nucl. Phys. B **489**, 679 (1997).

[20] H. A. Kramers and G. H. Wannier, Phys. Rev. **60**, 263 (1941).

[21] Originally we have formulated the TPVA by use of the corner transfer matrix renormalization group [T. Nishino and K. Okunishi, J. Phys. Soc. Jpn. **65**, 891 (1996)]. Here we employed the DMRG because the incommensurately and/or commensurately modulated phases require the use of the DMRG [A. Gendiar and A. Šurda, Phys. Rev. B **62**, 3960 (2000)].